Physicomechanical properties of wollastonite (CaSiO₃)/styrene butadiene rubber (SBR) nanocomposites

Aniruddha Chatterjee, Prashant S. Khobragade, Satyendra Mishra

University Institute of Chemical Technology, North Maharashtra University, Jalgaon-425001, MS, India
Correspondence to: A. Chatterjee (E-mail: aniruddha_chatterjee2006@yahoo.co.in) and S. Mishra (E-mail: profsm@rediffmail.com)

ABSTRACT: The purpose of this study was to investigate the effect of bare wollastonite (BW) and modified wollastonite (MW) nanorods into the styrene butadiene rubber (SBR). SBR nanocomposites were prepared by the incorporation of different wt % (0.3–4.5) of BW and MW nanorods. All nanocomposites were characterized by thermal gravimetric analyzer (TGA) and differential scanning calorimeter (DSC). The particle size and morphology of BW and MW nanorods were characterized by field-emission scanning electron microscope (FE-SEM), transmission electron microscope (TEM), and Fourier transform infrared (FTIR) spectrophotometer, while FE-SEM and AFM analyses were performed for BW/SBR and MW/SBR nanocomposites. The obtained results revealed the existence of stronger interaction between the SBR and MW nanorods into MW/SBR as compared to BW/SBR nanocomposites. FE-SEM and AFM images showed a perfect dispersion of the MW nanorods in SBR matrix at 3 wt % loading. Thermal stability of MW/SBR nanocomposites was also increased significantly by the addition of MW nanorods. © 2015 Wiley Periodicals, Inc. J. Appl. Polym. Sci. **2015**, *132*, 42811.

INTRODUCTION

The fillers have been more often used to fulfill functional roles,[1] such as increasing thermal,[2,3] mechanical,[4,5] physical, morphological, and dimensional stability of the polymer and composite structures.[6] Sometimes, agglomeration or lower surface area of micron-size filler usually causes decrease in strength, impact resistance, and processability of polymer composites. While all these problems can be solved by using nanofillers, the presence of active hydroxyl and alkoxyl functional groups on nanofillers makes it more acidic and hydrophilic in nature which leads to poor polymer–filler interaction between rubber hydrocarbon and nanofillers. However, ethoxy organosilane coupling agents significantly improve the filler–rubber interactions[7] into compounded rubber matrix which enhances the thermal and mechanical properties of the composites. In spite of tremendous research activities in the field of polymer nanocomposites during the last two decades, elastomeric nanocomposites are still in a stage of infancy as far as their application is concerned.

Researchers have already been used different fillers in different polymer matrices such as calcium carbonate,[8] fly ash, carbon nanotubes (CNTs),[9] multi-walled CNTs,[10] carbon black, nanoclays,[11] organomodified nanoclays,[12] wollastonite, alumina clay,[13] ZnO,[14] Fe₃O₄,[15] magnesium hydroxide,[16–18] calcium sulphate,[19–22] and Ca₃(PO₄)₂[23,24] to study the thermal, rheological, mechanical, morphological, and flame retardant properties of polymer composites and their filler interactions. Basically, the main purpose of addition of mineral fillers in polymers is to reduce the cost and to give extra functionality. Common polymer composites reinforcing fillers are often used in an extent above 30 wt % concentration, whereas in nanofillers hardly exceeds 10 wt % in concentration. Therefore, meeting desired combinations of different properties in an elastomeric nanocomposite at a very small concentration of filler is of great concern.[25]

Wollastonite is a form of naturally occurring white calcium silicate (CaSiO₃) mineral which is relatively hard material (Moh hardness 4.8) with a specific gravity of 2.9.[26] Because of its acicular nature (the aspect ratio is usually between 10 and 20), it is a promising reinforcement for thermoplastics. It has great industrial importance due to its acicular crystal habit, a relatively high-level hardness, high brightness and whiteness, low moisture, low oil absorption, and low volatile content. Meng and Dou[27] have reported the effect of pimelic acid-modified wollastonite particles on the β-iPP formation during the isothermal crystallization of the composite. While, very few research work has been done on wollastonite nanorods and its effect on thermal and mechanical properties of elastomers.[28] Since, no such effective outcome and hardly any importance have been given to the flexibility, tensile strength, modulus, and thermal stability of the rubber composites.

Further research is therefore necessary to develop rubber nanocomposites with improved thermal stability and mechanical properties (tensile strength, flexibility, and modulus) by melt intercalation method. The effects of nano-$CaCO_3$, fly ash, and modified montmorillonite (MMT) on mechanical, thermal, cross-linking, and morphological properties of styrene butadiene rubber (SBR) as well as silicon rubber nanocomposites have been reported in our previous works and found excellent improvement in mechanical and thermal properties of composites with certain increment in filler loadings.

In this work, we have synthesized wollastonite nanorods by hydrothermal microemulsion technique and modified by using silane coupling agent as a surface modifier. The nanorods of 0.3–4.5 wt % loading were then dispersed in SBR matrix to study the influence of wollastonite filler (with or without surface modifier) on physicomechanical properties of SBR nanocomposites.[29–38]

EXPERIMENTAL

Materials

Calcium nitrate $Ca(NO)_2$ and sodium metasilicate (Na_2SiO_3) were purchased from Rankem, Mumbai, India. Cetyl-trimethyl ammonium bromide (CTAB), tri-ethoxy vinyl silane (TEVS), and toluene were purchased from Sigma Aldrich, Mumbai, India. n-pentanol was purchased from Avra synthesis Pvt. Ltd., India and n-hexane was purchased from Merck specialties Pvt. Ltd. India. All these chemicals were of analytical grade. Double distilled and deionized water (DDIW) was used throughout the experiment.

Cold polymerized emulsion styrene butadiene rubber (SBR, Grade 1502) purchased from Astlett Rubber Inc. with a bound styrene of 23.5%, 0.35% volatile matter, 0.2% ash, 5.8% organic acid, 0.94 specific gravity, and mooney viscosity 52 mL (100 °C) was used along with additives namely stearic acid, zinc oxide (ZnO), zinc diethyl dithiocarbamets (ZDC), 2, 2′dibenzothiazyl disulfide (MBTS), phenyl-B-methyl amine (Vulconex), and sulfur were procured commercial grade from Bayer India Limited, Mumbai, India.

Synthesis of Wollastonite Nanorods

Wollastonite nanorods were synthesized in an autoclave reactor (Amar Equipment Pvt. Ltd., Mumbai, India) by water/oil (W/O) hydrothermal microemulsion process. For this purpose, $0.6M$ of $Ca(NO_3)_2$ and $0.6M$ of Na_2SiO_3 solutions were prepared separately in deionized water. Then 5 mL of $0.6M$ $Ca(NO_3)_2$ and 5 mL of $0.6M$ Na_2SiO_3, 3 gm CTAB as a surfactant, 4 mL n-pentanol as a co-surfactant were mixed in 65 mL n-hexane as an oil phase under ultrasonication (Chrom Tech, India) (irradiation of 5 s/pulse).[38] The reactant molar ratio of Ca^{2+}/SiO_3^{2-} was kept at $1.0M$. The obtained microemulsion was then transferred into a stainless-steel autoclave and heated up to 170 °C at 3 bar for 22 h under 200 rpm followed by cooling to room temperature. After completion of the reaction, the obtained suspension was filtrated and washed three times with 1 : 1 mixture of DDIW and ethanol. The resultant powder was dried at 60 °C for 48 h and calcined at 800 °C for 2 h in a muf-

fle furnace (Bio-Technics, India).[38] Finally, a white powder of wollastonite was obtained.

Surface Modification of Wollastonite Nanorods

TEVS was used for the modification of wollastonite nanorods. First desired contents of silane coupling agent, i.e., TEVS (5 phr w.r.t weight of wollastonite) were dissolved in acetone. Twenty grams of wollastonite nanorods were dispersed in silane–acetone mixture under mechanical stirring at 500 rpm. The mixture was then sonicated for 1 h and again stirred at 500 rpm at room temperature for 2 h. The dispersion was kept for overnight to react TEVS with wollastonite nanorods. Finally, surface-modified wollastonite nanorods were collected by filtration followed by vacuum dry at 100 °C for 12 h.[39]

Preparation of Wollastonite/SBR Nanocomposites

BW/SBR and MW/SBR nanocomposites with 0.3, 0.6, 0.9, 1.5, 2.1, 3, and 4.5 wt % loading of wollastonite nanorods were masticated on a laboratory size open two roll mixing mill followed by compression molding. Formulation for rubber compounds was as follows: SBR (100 g), stearic acid (3 g), ZnO (3 g), vulconex (1 g), ZDC (0.5 g), 2,2′ MBTS (0.5 g), sulfur (1.8 g), and wollastonite nanorods (variable). Rubber was masticated on two-roll mill for 2–3 min and then stearic acid was added into it to give flexibility to the raw rubber. After complete addition of stearic acid, ZnO was added followed by addition of MBTS and ZDC which act as an activator and accelerators. Further, mixing was done for 1–2 min. Later, vulconex was added as an antioxidant and after sufficient mastication, sulfur was added. At last wollastonite nanorods were added very carefully. The total compounding cycle was finished within 15 min and the friction ratio of this mixing mill was 1 : 1.2 during the mixing tenure. The compounded rubber was subjected in a compression molding for 40 min at 140 °C under 100 kg/cm^2 pressure to get square sheet [15 × 15 × 0.2 cm].

Characterization

Particle Size and Morphology Analysis. Particle size of wollastonite nanorods was measured by particle size analyzer (Malvern, ZS90 Nanoseries, Malvern, UK). Morphology of wollastonite-filled SBR nanocomposites was determined by using field-emission scanning electron microscope (S-4800 Hitachi High. Tec, Tokyo, Japan) operating at an accelerating voltage of 30 kV and transmission electron microscope (M200 Philips) with 75 μA filament current and 200 kV accelerating voltage. The particles diameter was also measured directly by FE-SEM and TEM. EDS spectra for analyzing elemental composition of wollastonite nanorods was recorded on spectrometer attached with the FE-SEM.

X-ray Diffraction (XRD) Analysis. Synthesized BW and MW nanorods were characterized by using X-ray diffractometer (Bruker D8 Advance, Berlin, Germany) in the range of 20–80°. The samples were placed vertically in front of the X-ray source. The detector was moving at an angle of 2θ while the sample was moving at an angle of θ at the wavelength $\lambda = 1.54$ Å (Cu Kα, a tube voltage 40 kV and tube current 25 mA).

Fourier Transform Infrared (FTIR) Spectroscopy Analysis. The FTIR absorption spectra of BW and MW nanorods were

recorded on FTIR-8000 spectrophotometer (Shimadzu, Tokyo, Japan) at room temperature keeping 25 scans per sample. The resolution of the measurements was $4\,cm^{-1}$ and recorded from 400 to $4000\,cm^{-1}$ wave number.

Differential Scanning Colorimetrty (DSC) Analysis. All composites were sealed in aluminum sample pans (5–10 mg) and their thermal behaviors were determined by using DSC-60 (Shimadzu, Tokyo, Japan). Indium was employed for temperature calibration and nitrogen gas with a flux of *ca* 50 mL/min was used to prevent oxidative degradation of samples. Thermograms were recorded within the range of -120 to $25\,°C$ at a heating rate of $10\,°C/min$. The inflection point of the slope of the heat capacity plot was taken as the glass transition temperature (T_g). All samples were run one time.

Thermogravimetric Analysis (TGA). Thermal degradation properties of VZ-SBR, BW/SBR_{1-7}, and MW/SBR_{1-7} were determined on TGA-50 (Shimadzu, Tokyo, Japan) thermogravimetric analyzer. Sample of 10 mg was put on an aluminum pan for TGA. The temperature programming was from 30 to $550\,°C$ at a heating rate of $10\,°C/min$ under a nitrogen atmosphere (50 mL/min) to avoid thermo-oxidative degradation. All samples were run one time.

Mechanical Properties. The mechanical properties such as tensile strength (TS), elongation at break (EB), and modulus at 300% (ME300) were measured per ASTM-D 412 using Universal testing machine (UTM 2302) supplied by R&D Equipment, Mumbai. Cross-head speed was 50 mm/min. Samples were of standard dumble shape.

Hardness was measured according to ASTM D2240 by an international rubber hardness degrees (IRHD) tester (Blue Steel Engineers Pvt. Ltd., Mumbai, India, Shore-A, Hardness Durometer, Model Std-A).

Specific Gravity
An analytical balance equipped with a stationary support for an immersion vessel above or below the balance pan was used for specific gravity measurement per ASTM D 792. Corrosion-resistant wire for suspending the specimen and sinker for lighter specimen with a specific gravity of <1 was employed. A beaker was used as an immersion vessel, the test specimen of convenient size was weighed in air, and then the specimen was suspended from a fine wire attached to the balance. The sample was completely immersed in distilled water. The weight of the specimen in water was determined (with sinker). The specific gravity of the specimen was calculated as follows:

$$\text{Specific gravity of specimen} = \frac{a}{(a+w)-b} \tag{1}$$

where $a =$ weight of specimen in air, $b =$ weight of specimen (with sinker) and wire in water, and $w =$ weight of totally immersed sinker and partially immersed wire.

Cross-Link Density
Cross-link density (n) of SBR nanocomposites was determined on the basis of rapid solvent-swelling measurements. The samples were swollen in toluene at $27\,°C$ for 72 h until equilibrium swel-

ling was reached. The cross-link density of SBR nanocomposites was calculated by application of Flory–Rhener equation:[40]

$$n = \frac{-[\ln(1-\Phi_r)+\Phi_r\chi\Phi_r^2]}{V_0[\Phi_r^{1/3}-(\Phi_r/2)]} \tag{2}$$

where Φ_r is the volume fraction of polymer in the swollen mass, V_0 is the molar volume of the solvent (106.2 for toluene), and χ is the Flory–Huggins polymer–solvent interaction term (the value of χ is 0.393 for toluene). The volume fraction of polymer, Φ_r, is calculated by the following expression:[41]

$$\Phi_r = \frac{(W_r/\rho_r)}{\left(\frac{W_r}{\rho_r}\right)+\left(\frac{W_s}{\rho_s}\right)} \tag{3}$$

where W_r and W_s are the weight of the rubber samples and the swollen rubber, respectively. ρ_r and ρ_s are the density of the rubber samples and density of the solvent, respectively.

Atomic Force Microscopy (AFM) Analysis
SBR nanocomposites morphology was examined by AFM methodology with a Scanning Probe Microscope Solver PRO (NT-MDT, Moscow, Russia) setup, at room temperature (23 °C). The height images were recorded using AFM taping mode, wherein the cantilever force was controlled to be large enough to explore the surface features, yet small enough to avoid the sample damage. The film surfaces were scanned by a rectangular silicon cantilever NSG10 (NT-MDT, Moscow, Russia) having a spring constant of 11.8 N/m and a resonance frequency of 234 kHz in a tapping mode. The scan area and speed were $5 \times 5\,\mu m^2$ and $10\,\mu m/s$, respectively.

Statistical Analysis
In the sections Mechanical Properties, Specific Gravity, and Cross-Link Density, all the analysis was performed in triplicate except the analysis of mechanical properties which was done five times. The means and standard deviation were calculated and plots are generated using Microsoft Office Excel.

RESULTS AND DISCUSSION

Structural Properties and Morphology of Wollastonite Nanorods

Figure 1 shows the XRD patterns of the obtained powders of BW and MW nanorods. Figure 1(a) showed the XRD pattern of the obtained powder after hydrothermal treatment at 200 °C for 22 h and identified as tobermorite (JCPDS card: No. 45-1480). It could be seen that there were numerous peaks and low background in the XRD pattern of the tobermorite powder. The shape of the strong diffraction peak at $2\theta = 27°$ indicated that the samples are fairly well crystallized. On the other hand, the patterns of the numerous low background in the XRD pattern also indicated that some residual calcium oxide (JCPDS card: No. 28-0775) component existed as an amorphous state. After calcination at 800 °C for 2 h, the phase of the powder transformed from tobermorite to monoclinic β-CaSiO_3 (JCPDS 84-0655), which can be identified from the XRD pattern in Figure 1(b). It can be seen that the sharp peaks with minor diffused background represented crystalline nature of wollastonite. Meanwhile, the XRD pattern of the sample did not reveal any other phase except monoclinic β-wollastonite.
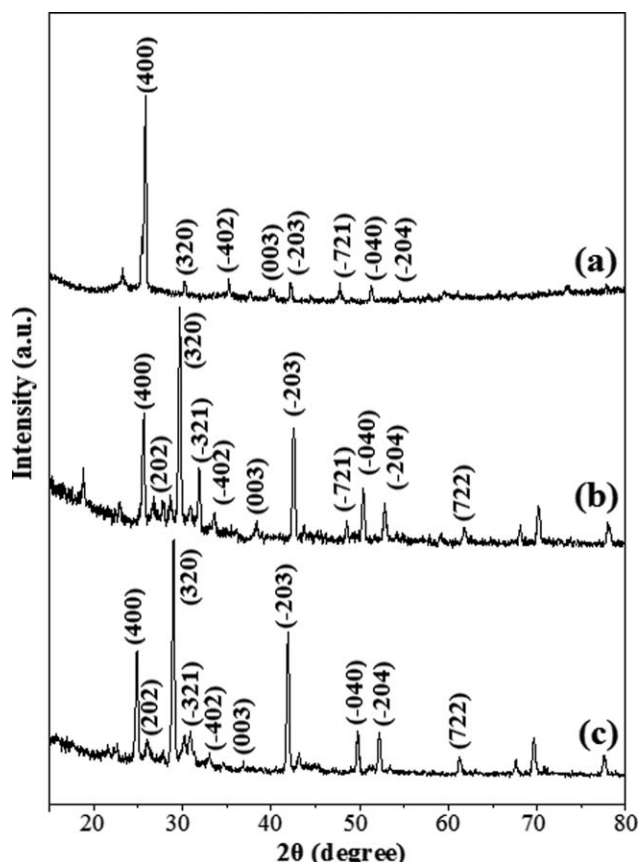
Figure 1. XRD diffraction pattern of (a) before calcination, (b) after calcination, and (c) TEVS-modified wollastonite nanorods.

The FE-SEM images of Figure 2(a–c) and TEM micrographs inset in Figure 2(c) indicated that the wollastonite nanorods has smooth surfaces with regular shapes of 30∼60 nm in diameter and up to 1 μm in length, while in micrographs not a single spherical nanoparticle was observed. The morphology and size of the nanorods were well preserved during the crystal phase transformation. This was also confirmed by particle size analyzer [Figure 2(d)]. The average particle diameter was slightly higher (120 nm) due to 1D structure of nanorods. The typical SAED pattern inset in Figure 2(a,b) of one single nanorod implies that the resultant tobermorite and β-CaSiO$_3$ nanorods were crystalline. The indexes of the spots in the SAED patterns indicate that the booth crystals are single-crystalline and grows along the (001) direction. This was further confirmed by EDS analysis [Figure 2(e)], which showed Ca, Si, and O peaks as well as relative quantities of these different elements.

From the results of the XRD (Figure 1) and FE-SEM (Figure 2), it can be concluded that hydrothermal microemulsion method is an effective way to obtain the β-CaSiO$_3$ nanorods. The size and size distribution in diameter of the nanorods were similar to the fibers prepared by Li et al.[37] and Lin et al.[38] These were profited from the function of the microemulsion in the reaction system, which served as nanoreactors and effectively controlled the particle size and size distribution, and inhibited the excess agglomeration of the nanorods in the process.

On the other hand, to determine the influence of surface modification of wollastonite powders, X-ray diffraction pattern of MW was also conducted [Figure 1(c)]. By the observation of XRD patterns, it can be concluded that hydrophilic BW nanorods showed higher aggregation [Figure 2(b)] than MW nanorods [Figure 2(c)]. After surface modification by using TEVS, an organic layer is deposited on the surfaces of nanorods and hydrophobic nature is developed on the surfaces which reduce aggregation between wollastonite nanorods [Figure 2(c)]. This is also confirmed by XRD pattern of both nanorods. In XRD pattern of BW nanorods [Figure 1(b)], the main diffraction planes at (400), (202), (320), and (040) at $2\theta = 25.62°$, $27.14°$, $29.42°$, and $51.20°$, respectively. Contrarily, in the case of MW nanorods, the same planes were shifted toward lower diffraction angle and showed the diffraction peaks at $2\theta = 23.74°$, $25.56°$, $28.67°$, and $50.38°$, respectively [Figure 1(c)]. This attributed to adsorption of TEVS on nanorod surfaces and creating a hydrophobic layer on the rods surfaces, which resulted in reduction of nanorods aggregates inset in Figure 2(c).

For further evidence, FTIR spectra of Figure 3(a) showed the high-frequency peaks in between the spectral range of 800–1250 cm^{-1} which assigned to asymmetric Si—O stretching could of SiO$_4$ tetrahedron.[26,39] The mid-frequency at 600–800 cm^{-1} could be attributed to both Si—O—Si bending and Si—O stretching vibrations, while the band obtained at low-frequency ranges (400–600 cm^{-1} originated from O—Si—O bending and Ca—O stretching.[26] The high-frequency peaks in the spectral range of 2850–3000 cm^{-1} were assigned to C—H stretching modes of alkanes (methyl group). On the other hand, for surface-modified wollastonite [Figure 3(b)], spectra's at 1680 and 1640 cm^{-1} were attributed to the C═C stretching vibration and band near 2850 cm^{-1} was attributed to the C—H stretching of vinyl and alkenes group (ethyl group). The significant difference between the nanorods before and after modification appeared at 1624 cm^{-1} that was due to C═C unsaturation in TEVS grafted to wollastonite surface.[39]

DSC Analysis of MW/SBR and BW/SBR Nanocomposites
Glass transition temperatures (T_g) of VZ-SBR, MW/SBR$_{1-7}$, and BW/SBR$_{1-7}$ nanocomposites are shown in Figures 4 and 5 and tabulated in Table I. Figure 4 showed that T_g of SBR nanocomposites were higher than VZ-SBR ($-65°C$). In Figure 4, T_g of MW/SBR nanocomposites constantly increased for MW/SBR$_{1-4}$ (-63 to $-55°C$), showed stability for MW/SBR$_{5-6}$ ($-53°C$) and again decreased in MW/SBR$_7$ ($-58°C$). Whereas in Figure 5, T_g of BW/SBR nanocomposites were gradually increased for BW/SBR$_{1-5}$ (-64 to $-56°C$) and then constantly decreased for BW/SBR$_{6-7}$ (-60 to $-62°C$). Overall, it is observed that T_g of MW/SBR is better than BW/SBR nanocomposites.[8] It means that at lower loading, the T_g shifted to higher temperature; moreover, the large difference in T_g is due to the uniform dispersion of modified wollastonite in SBR matrix. On the other hand at higher loading, decrement in T_g and increment of brittleness are due to the aggregation and increasing amount of wollastonite as filler. To understand the above phenomenon, there are few factors which influence the glass transition temperature (T_g), (1) the presence of crystalline wollastonite nanorods, (2) the TEVS chemically grafted onto the wollastonite
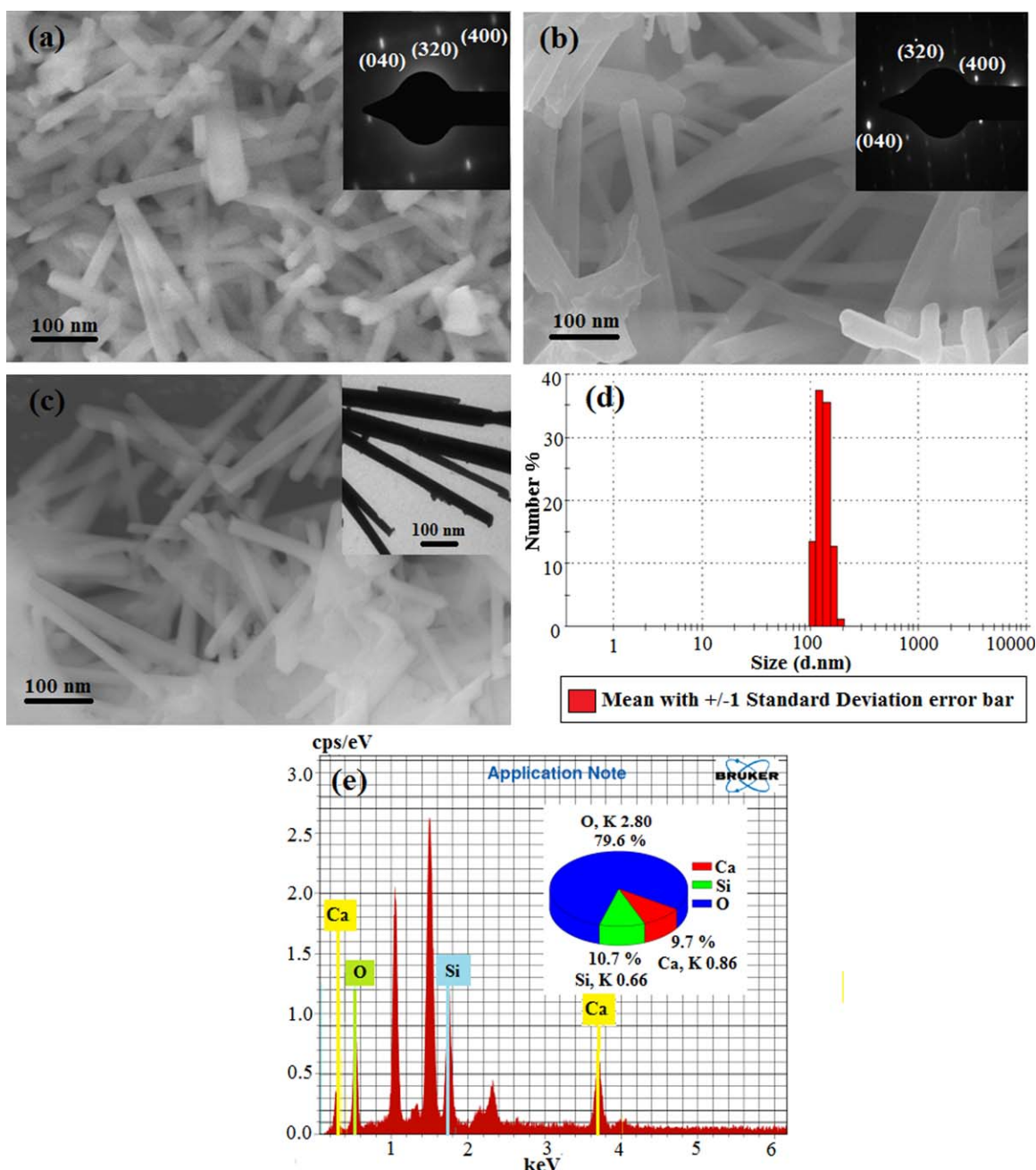
Figure 2. FE-SEM micrograph of (a) before calcination, (b) after calcination, (c) TEVS-modified wollastonite nanorods, (d) particle size analysis, and (e) EDS spectra of wollastonite nanorods. [Color figure can be viewed in the online issue, which is available at wileyonlinelibrary.com.]

nanorods, (3) compatibility of wollastonite nanorods as filler with SBR matrix, (4) dispersion and aggregation phenomena of wollastonite nanorods into SBR matrix, were taken under consideration. It has been well explained in our earlier work[39,42,44] as follows: first, TEVS as coupling agent chemically grafted onto wollastonite nanorods acting as a compatibilizer and brought individual wollastonite nanorods very easily without any agglomeration in between SBR chain segments, and dispersed uniformly. Second, presence of wollastonite nanorods as rigid filler phase, restricts the chain movements and as a consequence T_g of the nanocomposites initially increased.[42,43] Third, rather than aggregation, uniform dispersion of wollastonite nanorods

improved the filler–matrix interaction between wollastonite–SBR matrix.

Thermal Stability of MW/SBR and BW/SBR Nanocomposites
The thermal decomposition behavior of VZ-SBR, MW/SBR$_{1-7}$, and BW/SBR$_{1-7}$ nanocomposites were recorded and shown in Figures 6 and 7, respectively. The data available from TGA include onset degradation temperature (d_{on}), the temperature at which 5% degradation occurs; the offset degradation temperature (d_{off}) at which 80% degradation occurs; and the nonvolatile fraction at 550 °C denoted as percentage weight loss (W_L). The data of various nanocomposites were summarized in Table
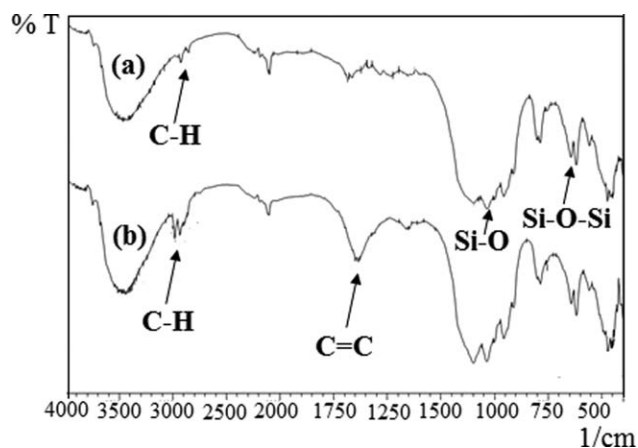
Figure 3. FTIR spectra of (a) bare wollastonite and (b) TEVS-modified wollastonite.

I. Thermal stability of the MW/SBR$_{1-7}$ nanocomposites was noticeably improved than that of the VZ-SBR matrix. The data of d_{on}, d_{off}, and W_L were shifted to higher side with enhancing the filler content in MW/SBR nanocomposites as compared to VZ-SBR.[8,44] The decomposition temperature was increased as much as 33 °C. The highest improvement of d_{on} = 33 °C was observed for MW/SBR$_6$. The origin of the noticeable increase in decomposition temperature is mainly attributed to uniform dispersion of wollastonite nanorods and strong interaction between the wollastonite nanorods and the SBR matrix as depicted in the SEM images in Figure 12.[42,43] It was also noticed that above 500 °C, MW/SBR$_{1,2}$ showed similar W_L as compared with VZ-SBR. The stability was observed for MW/SBR$_{3,4}$ and showed W_L about 99%. But at higher loading, MW/SBR$_{5-7}$ showed W_L about 98%, 97%, and 96%, respectively. This is mainly attributed to weak interaction between wollastonite nanorods and SBR matrix at higher loading and composed wollastonite as residue.
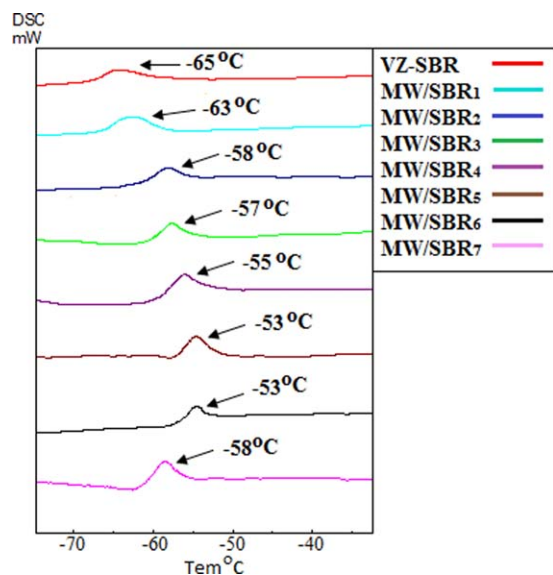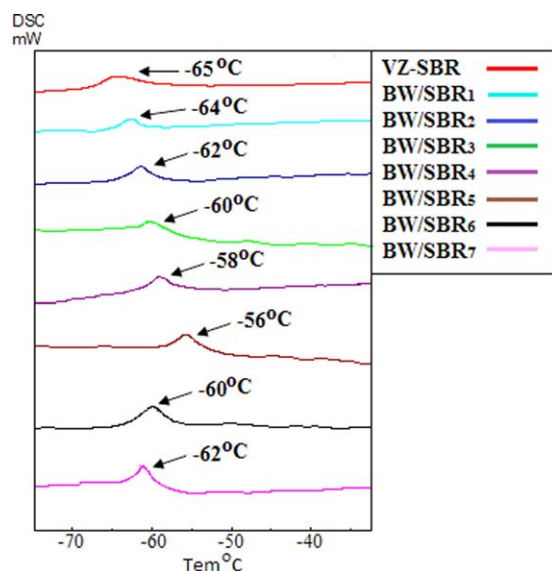

Figure 5. DSC thermograms of BW/SBR$_{1-7}$ nanocomposites. [Color figure can be viewed in the online issue, which is available at wileyonlinelibrary.com.]

On the other hand, steady improvement in thermal stability was observed for BW/SBR nanocomposites as compared with VZ-SBR (Figure 7). Thermal stability was increased up to 15 °C. BW/SBR$_5$ with 2.1 wt % wollastonite nanorods loading showed highest improvement on d_{on}. This improvement is mainly due to the crystalline nature of wollastonite nanorods. Further addition lowers down the dispersion of wollastonite nanorods in SBR matrix, i.e., % of aggregation increased in rubber matrix, which directly influence the thermal stability of BW/SBR nanocomposites (see Table I and FE-SEM images in Figure 11).

Figure 4. DSC thermograms of MW/SBR$_{1-7}$ nanocomposites. [Color figure can be viewed in the online issue, which is available at wileyonlinelibrary.com.]

Table I. DSC and TGA Results of BW/SBR$_{1-7}$ and MW/SBR$_{1-7}$ Nanocomposites

| Samples	T_{g1} (°C)	d_{on} (°C)	d_{off} (°C)	W_L (%)
VZ-SBR	−65(±1)	339(±5)	465(±5)	100(−1)
MW/SBR$_1$	−63(±1)	343(±5)	469(±5)	100(−1)
MW/SBR$_2$	−58(±1)	348(±5)	475(±5)	100(−1)
MW-SBR$_3$	−57(±1)	361(±5)	473(±5)	99(±1)
MW/SBR$_4$	−55(±1)	367(±5)	484(±5)	99(±1)
MW/SBR$_5$	−53(±1)	368(±5)	494(±5)	98(±1)
MW/SBR$_6$	−53(±1)	373(±5)	499(±5)	97(±1)
MW/SBR$_7$	−58(±1)	357(±5)	512(±5)	96(±1)
BW/SBR$_1$	−64(±1)	341(±5)	460(±5)	100(−1)
BW/SBR$_2$	−62(±1)	343(±5)	467(±5)	100(−1)
BW/SBR$_3$	−60(±1)	345(±5)	472(±5)	99(±1)
BW/SBR$_4$	−58(±1)	347(±5)	478(±5)	99(±1)
BW/SBR$_5$	−56(±1)	357(±5)	478(±5)	98(±1)
BW/SBR$_6$	−60(±1)	350(±5)	483(±5)	98(±1)
BW/SBR$_7$	−62(±1)	344(±4)	492(±5)	97(±1)
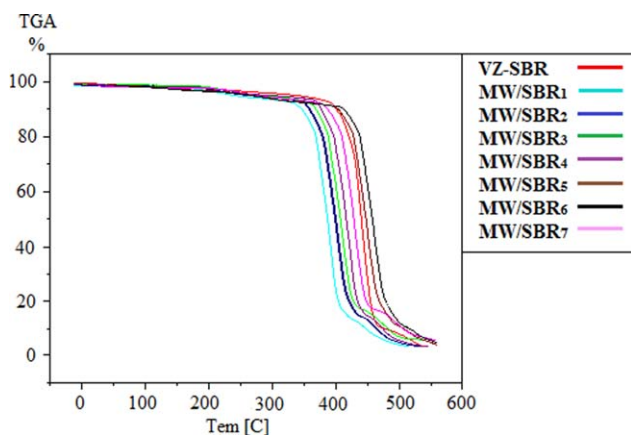
Figure 6. TGA curves of MW/SBR$_{1-7}$ nanocomposites. [Color figure can be viewed in the online issue, which is available at wileyonlinelibrary. com.]

Figure 8. Tensile strength and elongation at break of wollastonite/SBR nanocomposites [error bar represents 1 standard deviation (SD) with $n = 5$]. [Color figure can be viewed in the online issue, which is available at wileyonlinelibrary.com.]

Mechanical Properties

Tensile strength (TS), elongation at break (EB), modulus at 300% elongation (ME300), and hardness of BW/SBR and MW/SBR nanocomposites at various wollastonite wt % loading are shown in Figures 8 and 9. In Figure 8, it can be seen that the TS of BW/SBR and MW/SBR nanocomposites were shown same increasing trend up to 3 wt % loading. This was due to greater reinforcing interaction between nanofillers and chains in SBR matrix. However, the better TS was observed in case of MW/SBR nanocomposites. This indicated that good interaction between SBR and MW nanorods improved the compatibility between wollastonite–SBR matrix. In contrary, at higher loading (4.5 wt %), the TS of both SBR nanocomposites decreased due to agglomeration of the wollastonite nanorods [Figures 11(d) and 12(d)]. These may lead to less interfacial interaction between wollastonite and SBR matrix resulted in a reduction in TS of both SBR nanocomposites at 4.5 wt % loading.

It was also evident from Figure 8 that the EB of nanocomposites is increased up to 0.9 wt % of wollastonite loading and showed stability at 1.5 and 2.1 wt % and again decreased in 3 and 4.5 wt % loadings. At the early stage, due to proper dispersion of nanorods, the enhancement of elongation is the high
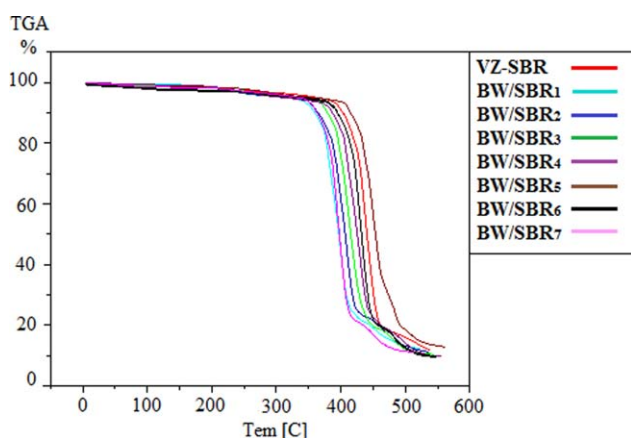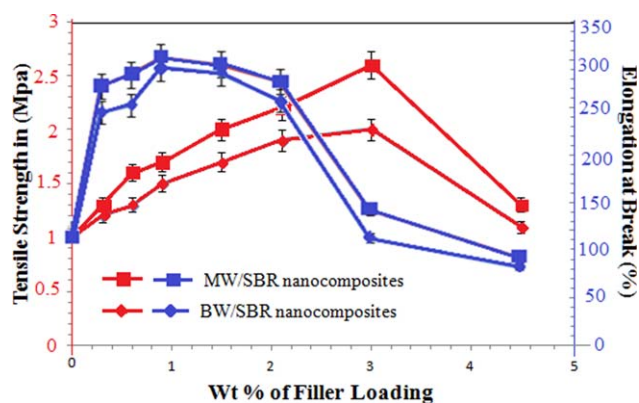
resistance exerted by well-dispersed wollastonite fillers against the chain deformation and the stretching resistance of the oriented rubber backbones in the galleries. In addition, an improvement in the mechanical properties can also be accounted on the basis of static adhesion strength as well as interfacial stiffness caused by the efficient stress transfer at the interface and elastic deformation originating from the increased wt % of wollastonite nanorods as filler. Overall EB is better in case of MW/SBR nanocomposites. The lower EB of BW/SBR nanocomposites is attributed to aggregation of nanorods as well as formation of weaker interfacial region between the unmodified filler surface and matrix resulting in development of cracks.[44] Besides, both nanocomposites showed constant increment in ME 300 (Figure 9) and maximum increment was observed at 3 wt % loading of wollastonite nanorods. This is due to high stiffness of the wollastonite at higher loading. In addition, the hardness of SBR nanocomposites (Figure 9) was increased in the same fashion as ME 300 of the SBR nanocomposites.

Figure 10 shows the specific gravity of all SBR nanocomposites. There is continuous increment in specific gravity for all
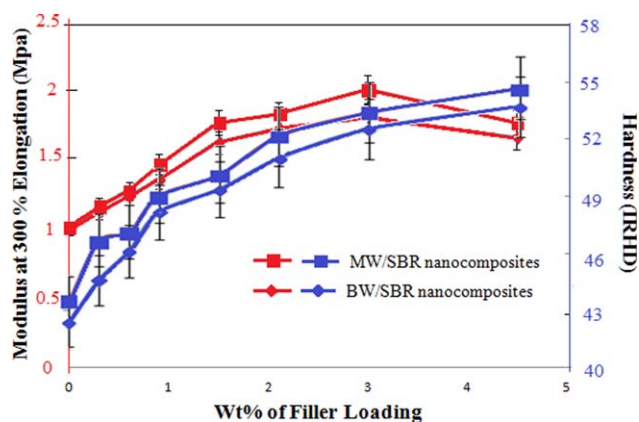

Figure 7. TGA curves of BW/SBR$_{1-7}$ nanocomposites. [Color figure can be viewed in the online issue, which is available at wileyonlinelibrary.com.]

Figure 9. Modulus and hardness of wollastonite/SBR [error bar represents 1 standard deviation (SD) with $n = 5$ and 3]. [Color figure can be viewed in the online issue, which is available at wileyonlinelibrary.com.]
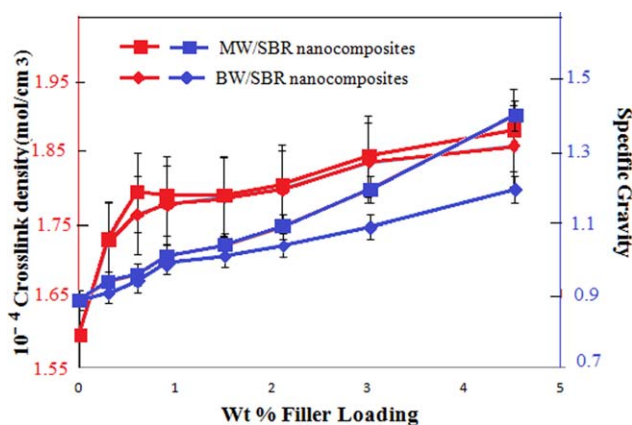
Figure 10. Specific gravity and cross-link density of wollastonite/SBR nanocomposites [error bar represents 1 standard deviation (SD) with $n = 3$]. [Color figure can be viewed in the online issue, which is available at wileyonlinelibrary.com.]

nanocomposites in comparison to VZ-SBR (0.94). The increment in specific gravity is due to addition of nanorods as filler in matrix, which bring the chains closer in order to reduce the free volume to greater extent in between cross-linked chains. In contrary, there is no significant difference in cross-link density is observed for both nanocomposites (Figure 10). This indicated that the cross-link density of SBR does not effect on properties of SBR nanocomposites. This can be concluded that the change in properties of the nanocomposites was due to the wollastonite loading as well as the interaction between the wollastonite and SBR matrix.

Surface Morphology and Dispersibility of Nanorods in MW/SBR and BW/SBR Nanocomposites Using FE-SEM and AFM

Based on our preliminary data and previous works, we profit from the possibility of using modified fillers to investigate the dispersibility of rigid phase in the soft phase, as well as to control the physicomechanical properties and surface morphology of nanocomposites; and to explore this, we have done detail investigation on surface morphology of SBR nanocomposites using FE-SEM and AFM. FE-SEM and AFM can provide qualitative information about dispersibility of various components, internal structures, and structural defects.

Figures 11–14 show the FE-SEM and AFM images of BW/SBR and MW/SBR nanocomposites with 0.6, 1.5, 3, and 4.5 wt % loading of wollastonite nanorods as filler. The inferior performance of BW/SBR nanocomposites is visualized in FE-SEM studies and attributed to the poor rubber–filler interaction than MW/SBR nanocomposites. There are no such changes observed in FE-SEM images of BW/SBR [Figure 11(a,b)] and MW/SBR [Figure 12(a,b)] nanocomposites with 0.6, 1.5 wt % filler loadings. On the other hand, at 3 wt % loading in MW/SBR nanocomposite [Figure 12(c)], perfect distribution of nanorods is observed than that of BW/SBR nanocomposite [Figure 11(c)]. Besides, at higher filler loading (4.5 wt %), BW/SBR nanocomposite [Figure 11(d)] showed higher agglomeration than MW/SBR nanocomposite [Figure 12(d)]. The above improvement with modified nano-wollastonite is due to the hydrophobic nature generated by silane coupling agent on the surface of nano-wollastonite, enhancing the dispersibility with higher dispersion and less agglomeration.[39,42,44]
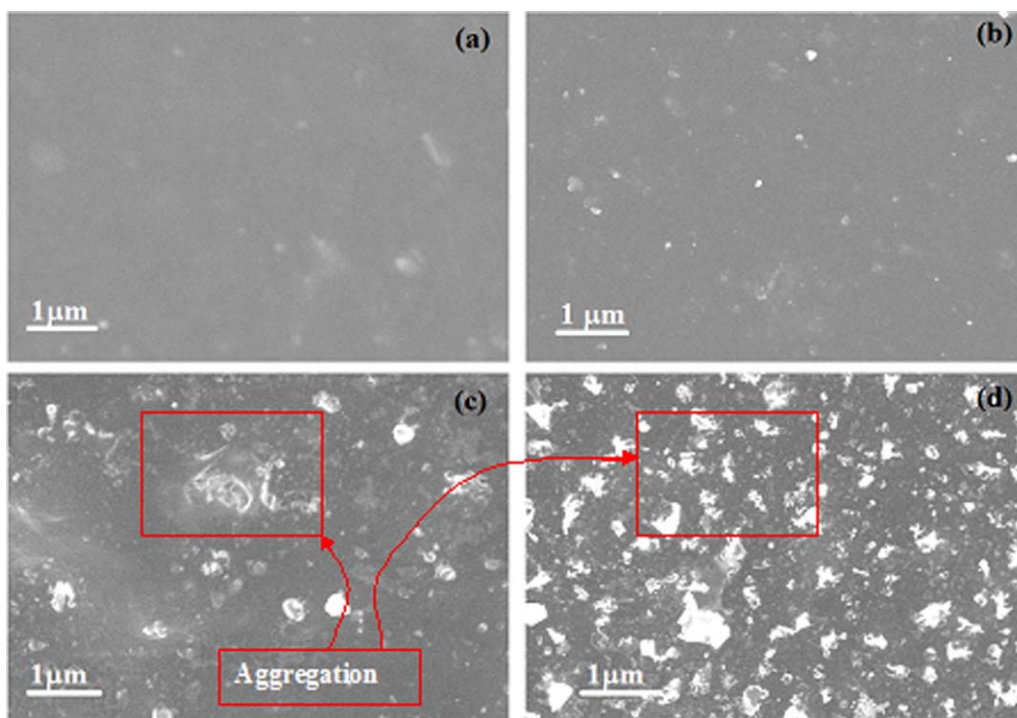

Figure 11. FE-SEM images of BW/SBR nanocomposites of (a) 0.6 wt %, (b) 1.5 wt %, (c) 3 wt %, and (d) 4.5 wt % wollastonite loading. [Color figure can be viewed in the online issue, which is available at wileyonlinelibrary.com.]
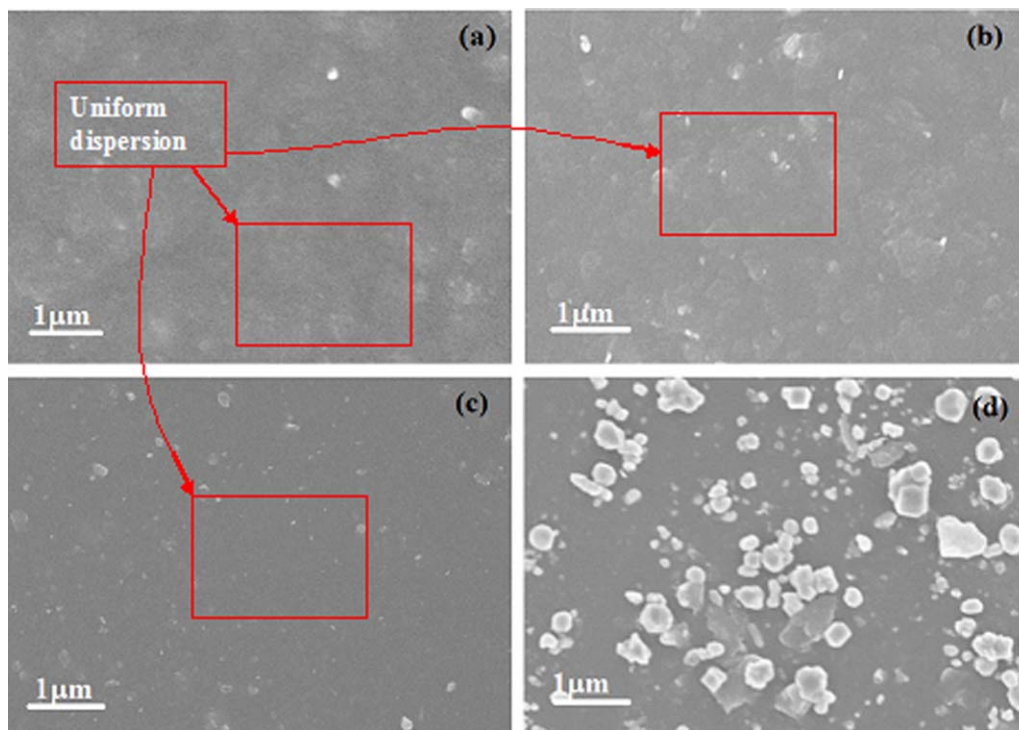
Figure 12. FE-SEM images of MW/SBR nanocomposites of (a) 0.6 wt %, b) 1.5 wt %, (c) 3 wt %, and (d) 4.5 wt % wollastonite loading. [Color figure can be viewed in the online issue, which is available at wileyonlinelibrary.com.]

Figure 13. AFM images of BW/SBR nanocomposites of (a) 0.6 wt %, (b) 1.5 wt %, (c) 3 wt %, and (d) 4.5 wt % wollastonite loading. [Color figure can be viewed in the online issue, which is available at wileyonlinelibrary.com.]
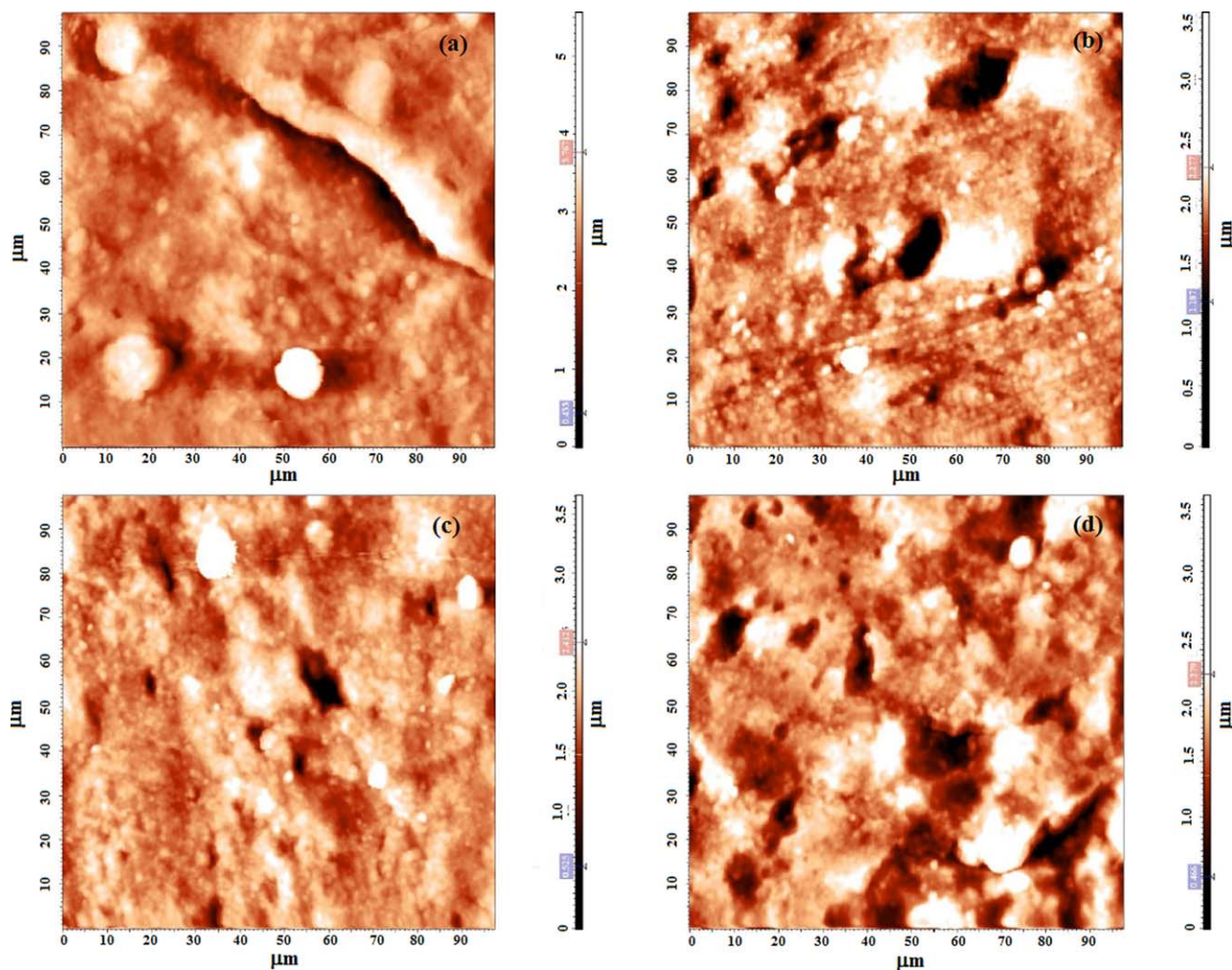
Figure 14. AFM images of MW/SBR nanocomposites of (a) 0.6 wt %, (b) 1.5 wt %, (c) 3 wt %, and (d) 4.5 wt % wollastonite loading. [Color figure can be viewed in the online issue, which is available at wileyonlinelibrary.com.]
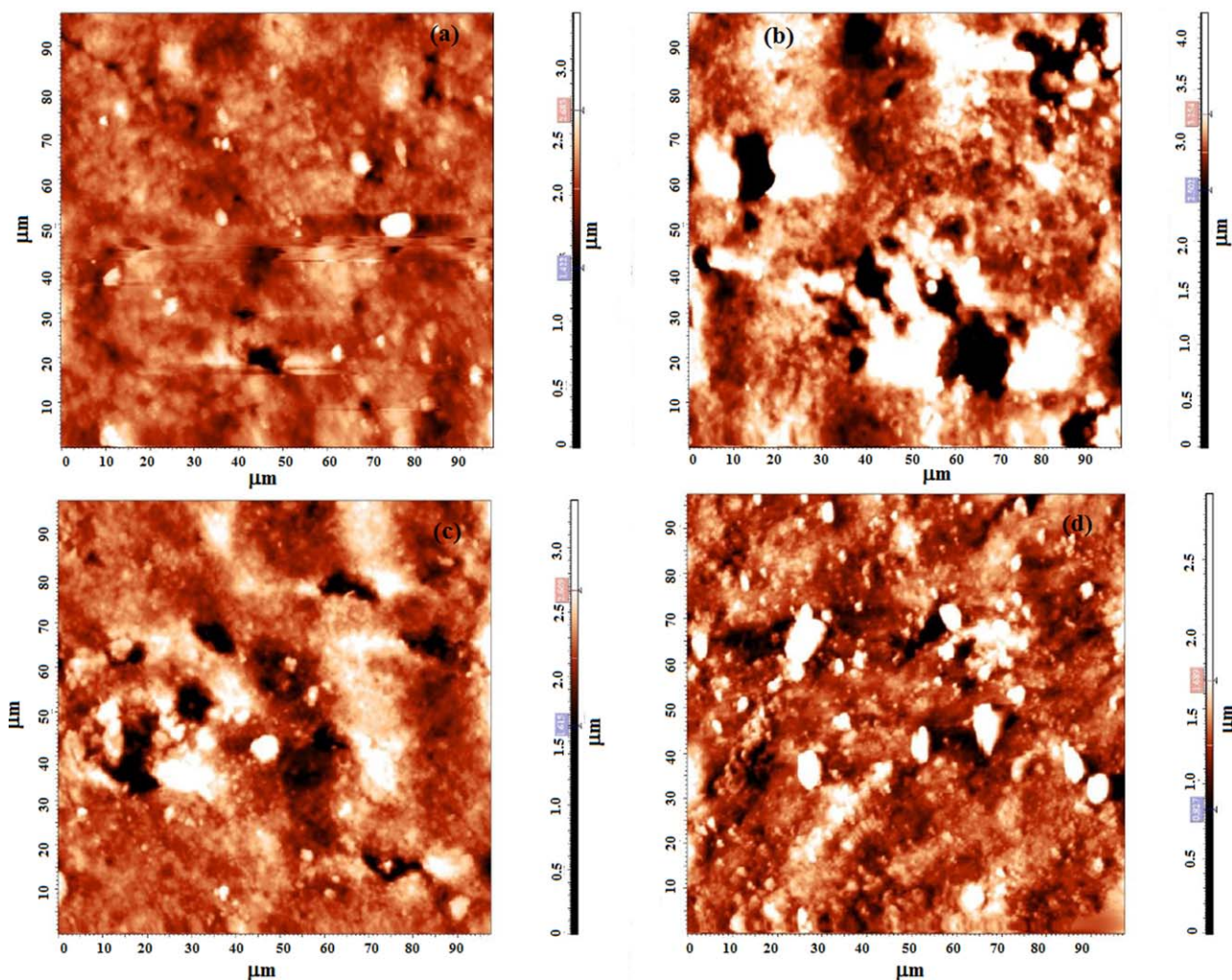
Particle dispersibility and surface morphology of BW/SBR and MW/SBR nanocomposites are further studied by AFM analysis [Figures 13 and 14]. Generally, the scales of AFM phase images are set so that the harder phase induces a higher phase offset and appears brighter, whereas the softer phase appears darker.[43,44] Therefore, in this study, the white or bright regions of the AFM images correspond to the hard phase, whereas the brown or darker regions are representative of soft rubber phase. Figures 13 and 14 show the tapping mode/phase images of BW/SBR and MW/SBR nanocomposites, respectively. In case of BW/SBR nanocomposites, at lower loading (0.6 and 1.5 wt %), the wollastonite nanorods are uniformly distributed [Figure 13(a,b)] indicating strong intercalation between wollastonite and SBR with higher content of soft segments (brown region) which is higher than 0.3 and 4.5 wt % loading of BW nanorods [Figure 13 (c,d)]. On the other hand, 0.6, 1.5, and 3 wt % loading of MW nanorods [Figure 14 (a–c)], MW/SBR nanocomposites show the highest segment of soft region as compare to 4.5 wt % of MW nanorods loading [Figure 14(d)]. Higher percentage of filler aggregation with high content of hard segments (white

region) is observed in BW/SBR than that of MW/SBR nanocomposites.

CONCLUSIONS

Based on the above investigation, the effect of wollastonite nanorods (before and after modification by TEVS) in SBR rubber, the following conclusions can be drawn: SBR rubber shows significant improvement in physicomechanical properties with optimum percentage (3 wt %) of wollastonite nanorods as filler. Wollastonite contributes good compression set properties which are very important for industrial application of SBR. Surface modification of wollastonite nanorods by TEVS improved the thermal and mechanical properties in a remarkable extent due to uniform dispersion of MW nanorods in SBR matrix. MW/SBR nanocomposites with 2.1 and 3 wt % loading have shown excellent mechanical properties and thermal stability. The optimum loading of MW nanorods is found to be 3 wt %. Further filler loading shows decrement in thermal stability and mechanical properties and this could be attributed to agglomeration of

wollastonite nanorods in SBR matrix. Since, there is high amount agglomerate in high filler dosage composites, these agglomerates played the role of an obstacle to molecular chain movement of the SBR, thereby initiating failure under stress. Same results are observed in case of BW/SBR nanocomposites, but overall properties are better for MW/SBR nanocomposites. These properties of MW/SBR nanocomposites are remarkably superior to those of pristine rubber or their conventional counterparts. Thus, preparation of SBR nanocomposites by reinforcement of MW nanorods is an excellent method to obtain well-dispersed nanorods than that of BW nanorods. This opens the way to a wider industrial utilization of MW nanorods.

REFERENCES

1. Svab, I.; Musil, V.; Jurkin, T.; Smit, I. *Polym. Eng. Sci.* **2007**, *47*, 2145.

2. Das, A.; Costa, F. R.; Wagenknecht, U.; Heinrich, G. *Eur. Polym. J.* **2008**, *44*, 3456.

3. Mishra, S.; Shimpi, N. G. *J. Sci. Ind. Res.* **2005**, *64*, 744.

4. Paul, K. T.; Pabi, S. K.; Chakraborty, K. K.; Nando, G. B. *Polym. Compos.* **2009**, *30*, 1647.

5. Frohlich, J.; Niedermeier, W.; Luginsland, H. D. *Compos. Part A Appl. Sci. Manufac.* **2005**, *36*, 449.

6. Mishra, S.; Mukherji, A. *J. Sci. Ind. Res.* **2006**, *65*, 582.

7. Praveen, S.; Chattopadhyay, P. K.; Albert, P.; Dalvi, V. G.; Chakraborty, B. C.; Chattopadhyay, S. *Compos. Part A Appl. Sci. Manufac.* **2009**, *40*, 309.

8. Mishra, S.; Shimpi, N. G.; Patil, U. D. *J. Polym. Res.* **2007**, *14*, 449.

9. Sui, G.; Zhong, W. H.; Yang, X. P.; Yu, Y. H.; Zhao, S. H. *Polym. Adv. Technol.* **2008**, *19*, 1543.

10. Girun, N.; Ahmadun, F. R.; Rashid, S. A. *Fullerene Nanotube Carb. Anoestrus* **2007**, *15*, 207.

11. Ghasemi, I.; Karrabi, M.; Mohammadi, M.; Azizi, H. *Exp. Polym. Lett.* **2010**, *4*, 62.

12. Mishra, S.; Shimpi, N. G.; Mali, A. D. *Macromol. Res.* **2012**, *20*, 44.

13. Mohamad, N.; Muchtar, A.; Ghazali, M. J.; Mohd, D. H.; Azhari, C. H. *Eur. J. Sci. Res.* **2008**, *24*, 538.

14. Kalaee, M.; Akhlaghi, S.; Mazinani, S.; Sharif, A.; Jarestani, Y. C.; Mortezaei, M. *J. Therm. Anal. Calorim.* **2012**, *110*, 1407.

15. Mohammadi, A.; Barikani, M.; Barmar, M. *J. Mater. Sci.* **2013**, *48*, 7493.

16. Mishra, S.; Sonawane, S. H.; Singh, R. P.; Patil, K.; Bendale, A. *J. Appl. Polym. Sci.* **2004**, *94*, 116.

17. Sonawane, S. S.; Mishra, S.; Shimpi, N. G. *Polym. Plast. Technol. Eng.* **2010**, *49*, 38.

18. Shimpi, N. G.; Sonawane, H. A.; Mali, A. D.; Mishra, S. *J. Reinf. Plast. Compos.* **2013**, *60*, 935.

19. Mishra, S.; Sonawane, S.; Mukherji, A.; Mrthutinjaya, H. C. *J. Appl. Polym. Sci.* **2006**, *100*, 4190.

20. Mishra, S.; Mukherji, A.; Sharma, D. K. *Polym. Plast. Technol. Eng.* **2006**, *45*, 1191.

21. Mishra, S.; Shimpi, N. G. *J. Appl. Polym. Sci.* **2007**, *104*, 2018.

22. Mishra, S.; Shimpi, N. G.; Verma, J. *Polym. Plast. Technol. Eng.* **2009**, *48*, 997.

23. Mishra, S.; Mukherji, A. *J. Appl. Polym. Sci.* **2007**, *103*, 670.

24. Mishra, S.; Shimpi N. G.; Sonawane, S. S. *Polym. Plast. Technol. Eng.* **2009**, *48*, 265.

25. Socrates, G. Infrared and Raman Characteristic Group Frequencies Tables and Charts, 3rd ed.; John Wiley & Sons Ltd., Chichester, England, ISBN: 978-0-470-09307-8, **2001**.

26. Luyt, A. S.; Dramicanin, M. D.; Antic, Z.; Djokovic, V. *Polym. Test.* **2009**, *28*, 348.

27. Meng, M. R.; Dou, Q. *Mater. Sci. Eng. A Struct. Mater.* **2008**, *492*, 177.

28. Meng, L. X.; Zang, Y.; Wang, F.; Zhang, Z.; Zhang, R.; Zhu, F. *Adv. Mater. Res.* **2011**, *217*, 286.

29. Qiu, Y.; Batchelor, S. D.; Jack, P. R.; McCord, M. G. *Compos. Sci. Technol.* **2000**, *60*, 2731.

30. Dasari, A.; Sarang, S.; and Misra, R. D. K. *Mater. Sci. Eng. A Struct. Mater. Prop. Microstruct. Process* **2004**, *368*, 191.

31. Hadal, R. S.; Dasari, A.; Rohrmann, J.; Misra, R. D. K. *Mater. Sci. Eng. A Struct. Mater. Prop. Microstruct. Process* **2004**, *372*, 296.

32. Dasari, A.; Misra, R. D. K. *J. Acta Mater.* **2004**, *52*, 1683.

33. Misra, R. D. K; Hadal, R.; Duncan, S. J. *J. Acta Mater.* **2004**, *52*, 4363.

34. Smit, I.; Musil, V.; Svab, I. *J. Appl. Polym. Sci.* **2004**, *91*, 4072.

35. Gai, G. S.; Yang, Y. F.; Fan, S. M.; Cai, Z. F. *Powder Technol.* **2005**, *153*, 153.

36. Svab, I.; Musil, V.; Leskovac, M. *Acta Chim. Slovenica* **2005**, *52*, 264.

37. Li, X.; Chang, J. *Chem. Lett.* **2004**, *331*, 458.

38. Lin, K.; Chang, J.; Lu, J. *Mater. Lett.* **2006**, *60*, 3007.

39. Chatterjee, A.; Mishra, S. *J. Polym. Res.* **2013**, *20*, 249.

40. Flory, P. J. Principles of Polymer Chemistry; Cornell University Press: Ithaca, New York, **1953**, p 576.

41. Avalos, F.; Ortiz, J. C.; Zitzumbo, R.; Lopez-Manchado, M. A.; Verdejo, R.; Arroyo, M. *Eur. Polym. J.* **2008**, *44*, 3108.

42. Chatterjee, A.; Mishra, S. *Macromol. Res.* **2013**, *21*, 474.

43. Chatterjee, A.; Mishra, S. *Particulology* **2012**, *11*, 760.

44. Mishra, S.; Chatterjee, A.; Singh, R. P. *Polym. Adv. Technol.* **2011**, *22*, 2571.